Department of Physics and Astronomy
Heidelberg University

Bachelor Thesis in Physics
submitted by

Simon Marcus Heidrich

born in Pforzheim (Germany)

2022

Recommissionig of the Hyper-EBIT by measuring x-ray spectra of highly charged ions

This Bachelor Thesis has been carried out by Simon Marcus Heidrich at the
Max Planck Institute for Nuclear Physics
under the supervision of
Priv. Doz. Dr. Sven Sturm

Abstract

Electron beam ion traps (EBIT) are experimental setups for the production, analysis and extraction of highly charged ions (HCI). High precision measurements of fundamental constants, like the g factor in the Penning-trap experiment ALPHATRAP, benefit from the properties of HCI. For inner shell electrons in heavy HCI, the electric field that the electron experiences close to the nucleus reaches values up to 10^{-16}V/cm. Investigating this strong interaction by measuring the properties of the bound electron therefore allows to test QED in extreme conditions. An EBIT capable to inject hydrogenlike HCI up to uranium into the ALPHATRAP Penning-trap setup would allow these tests. In the scope of this thesis the Hyper-EBIT, intended to provide this capability in the future, was recommissioned. After a long shutdown all of the Hyper-EBITs critical components were tested. Further the space charge compensation of the beam was determined through the study of dielectric recombination of He-like to O-like argon ions. In the process the successful operation at moderate beam energies of 7 keV and beam currents of up to 120 mA was demonstrated. This serves as preparations for the aimed beam energies of 300 keV, as the necessary high voltage components are currently under development.

Zusammenfassung

Eine Elektronenstrahl-Ionenfalle (EBIT, engl.: *electron beam ion trap*) ist als experimenteller Aufbau dafür konzipiert, hochgeladene Ionen (HCI, engl.: *highly charged ions*) zu produzieren, zu analysieren und auszustoßen. Hochpräzisions-Messungen fundamentaler physikalischer Konstanten, wie etwa dem g-Faktor im Penningfallen-Experiment APLPHATRAP, profitieren von den Eigenschaften HCIs. Die von inneren Schalenelektronen erfahrenen elektrischen Felder nahe am Kern eines HCI können bis zu 10^{-16}V/cm erreichen. Diese starke Interaktion anhand der Eigenschaften des gebundenen Elektrons zu untersuchen, erlaubt einen Test der QED (engl.: *quantum electro dynamics*) unter extremen Bedingungen. Eine EBIT mit der Fähigkeit heliumartige HCI -bis zu Uran- in die ALPHATRAP Penningfalle einzubringen würde dies ermöglichen. Im Rahmen dieser Arbeit wurde die Hyper-EBIT, welche gerade diesen Zweck in Zukunft erfüllen soll, wieder in Betrieb genommen. Nachdem diese lange Zeit stillgelegt war, konnten zunächst alle kritischen Komponenten getestet werden. Zudem wurde der Beitrag der Raumladung des Elektronenstrahls durch die Analyse von dielektrischer Rekombinationen in helium- bis sauerstoffartiges Argon bestimmt. Gleichzeitig konnte die tadellose Funktionstüchtigkeit bei moderaten Strahlenergien von 7 keV und Strahlströmen von bis zu 120 mA unter Beweis gestellt werden. All dies dient als Vorbereitung für den Betrieb bei angestrebten 300 keV Strahlenergie, während die dafür nötigen Hochspannungskomponenten noch in Entwicklung sind.

Contents

1 Introduction

Although our nearest environment mostly consists of neutral atoms or lowly charged ions, in the perspective of the universe this form of matter is not representative. Highly charged ions (HCI) make up the majority of mass in the universe in the form of plasma [1]. The significance of HCI in astrophysics, nuclear and plasma physics is therefore self evident. A little less obvious might be their relevance for fundamental physics and specifically their application for tests of the standard model (SM) of physics. Quantum electrodynamics (QED) is the first and most thoroughly tested quantum field theory of the SM, formalising the interaction of charged particles by photon exchange. In hydrogenlike high-Z elements the electron can experience electric field strengths of up to 10^{16} V/cm [2]. Such systems are of particular interest to high-precision measurements testing QED. As they are inherently well defined which is why the theoretical models achieve very accurate calculations. One example is the measurement of the gyromagnetic factor (g factor) in the ALPHATRAP Experiment [3]. Other Penning-trap experiments like Pentatrap [4] or Smiletrap [5] perform high-precision mass measurements making use of the properties of HCI.

In order to make HCI available for laboratory analysis, an instrument tailored for the production of HCI is required. As a variation on the concept of Electron Beam Ion Sources (EBIS) the first Electron Beam Ion Trap (EBIT) was developed in 1986 [6]. Since then, this laboratory instrument proved to be well suited for the production, storage, excitation and direct analysis of a wide range of HCI.
By magnetically compressing a stream of electrons originating from a heated cathode, a dense electron beam is formed inside the EBIT. This beam ionizes atoms in the center stepwise through electron impact, trapping the ions within an electrostatic potential. High charge states only become accessible if the electron beam energy exceeds the binding energies of the respective charge state.

Many EBIT designs, differing in orientation, size, magnetic field strength, electron beam energy and current as well as the cooling method were constructed and operated all over the globe [7]. Here at the Max Planck Institute for Nuclear Physics (MPIK) many different EBITs are in use. The newest kind are the versatile Heidelberg Compact EBITs (HC-EBIT) [8]. Both the ALPHA- and Pentatrap Penning-trap experiments are supplied with charged ions by HC-EBITs. For extremely highly charged ions ALPHATRAP is supplied by the Heidelberg EBIT (HD-EBIT).

As the production of bare uranium U^{92+} in an EBIT had been demonstrated by R. E. Marrs in 1994 [9], the HD-EBIT was designed to replicate this [10]. Though the necessary beam energies of up to 300 keV, proved to be out of reach. Discharges in the vacuum between the gun and trumpet electrode showed to be the limiting factor. Nevertheless, by reaching beam energies of up to 100 keV and currents of 500 mA [11] it is able to

produce a wide range of HCI and was involved in many precision measurements.

This thesis focuses on the Hyper-EBIT, the destined successor to the HD-EBIT which will push for greater beam energies of 300 keV. Once these energies are reached, ALPHATRAP aims to perform g-factor measurements and other tests with H-like (hydrogenlike) lead ($^{208}Pb^{81+}$) and beyond. After a long shutdown period, the recommissioning of the Hyper-EBIT was at the heart of this thesis. To demonstrate the beam production and trapping capabilities, spectroscopy of resonant recombinations in Argon ions was performed. This noble gas was chosen for it's well known resonance energies of the KLL dielectric recombination.

In the following, the underlying physics are presented and explained in Chapter 2. These general concepts are then specified to the actual experimental setup in Chapter 3. Afterwards, the results of the measurements are presented in Chapter 4 before ending with a general outlook on the topic in Chapter 5.

2 Theoretical foundations

2.1 Quantum mechanical basics

Since Rutherford's general description of an atom its indivisibility has been rightfully thrown overboard. Its composition of electrons and the nucleus, which consists out of neutrons and protons, became well known. Also the spectroscopy of various elements was carried out by Bunsen and Kirchhoff in Heidelberg. Their findings could be largely explained by the Bohr atomic model, a semi-classical description of the electron movement within the atom. Using classical mechanics one receives closed orbits of certain radii, of which the smallest one for the hydrogen atom later was named Bohr radius $a_0 = \frac{4\pi\epsilon_0\hbar^2}{m_e e^2}$. Nonetheless many phenomena could not be explained with this model and furthermore on exact examination, the spectral frequencies didn't match the values predicted by the Bohr model. This could be resolved by the introduction of a quantum mechanical description of the atom.

2.1.1 Hydrogen like atoms

Ions with only one bound electron are generally called hydrogenlike (H-like) atoms, as their electron configuration corresponds to that of a neutral hydrogen atom. Their quantum mechanical description is presented in this section.

The Schrödinger equation

$$i\hbar\frac{\partial\psi(\mathbf{r},t)}{\partial t} = \hat{H}\psi(\mathbf{r},t), \tag{2.1}$$

with the imaginary unit i and $\hbar$ as the reduced Planck constant, forms the solid basis of quantum mechanics. $\psi(\mathbf{r},t)$ represents the wave function of the particle, as its absolute square value $|\psi(\mathbf{r},t)|^2$ is the probability density to find it at given space and time. Together with the Hamiltonian $\hat{H}$ generally given by

$$\hat{H} = \hat{V}_{\text{pot}} - \frac{\hbar^2}{2m}\Delta, \tag{2.2}$$

it describes the time evolution of a system of a particle with mass m using the operator for the potential energy $\hat{V}_{\text{pot}}$ as well as the Laplace operator $\Delta = \partial_x^2 + \partial_y^2 + \partial_z^2$. The eigenvalues of the Hamiltonian are the energy-levels of the system which generally are of interest in atomic physics.

To describe the atom in this non-relativistic way, three more steps are required. Firstly, the Hamiltonian for the simplified model of a point-like nucleus of charge $+Ze$ with mass m_1 and the electron of mass m_2 and charge $-e$ is inserted. Then the motion of the whole

atom is separated from the relative motion of electron and nucleus by introducing the reduced mass $\mu = \frac{m_1 m_2}{m_1+m_2}$. Lastly, as the problem resembles a radial symmetry, the angular and radial components are separated and the quantum numbers n, l and m_l are introduced. This results in the same energy-levels already presented by the Bohr model,

$$E_n = -Ry^* \frac{Z^2}{n^2} \qquad n = 1, 2, ... \qquad \text{with} \qquad Ry^* = \frac{\mu e^4}{8\epsilon_0^2 h^2}, \tag{2.3}$$

the reduced Rydberg constant $Ry^* \approx 13.6$ eV.

This formalisation needs to be adjusted for relativistic effects using the Dirac equation, which also introduces the concept of the electron spin. A property of the electron responsible for the magnetic moment μ_s of the the electron, resulting in a further set of quantum numbers s and m_s. Therefore we arrive at the **notation**

$$n\,^{2s+1}L_j \qquad L = \{S, P, D, F, ...\} \text{ for } l = \{0, 1, 2, 3, ...\}$$

for the unique states of the atom. $n = 1, 2, ...$ still denotes the principal energy level, while the index $2s+1$, called multiplicity, gives the number of fine structure components of this state. According to the z-projection of orbital angular momentum and quantum number l the state is described by L. The total electronic angular momentum $\vec{j} = \vec{l} + \vec{s}$ results in the quantum number j as the lower right index.

Effects of QED, like the Lamb shift from the interaction with virtual particles, need to be considered for a complete description as well. Many of these effects scale with quadratic, cubic or even higher powers of the atomic number Z times the **fine structure constant** $\alpha = \frac{e^2}{4\pi\epsilon_0 \hbar c}$. Therefore, heavy H-like ions are of particular interest for comparison of these contributions to those predicted by QED theory. Furthermore the hyperfine structure summarizes the effects due to interaction between the electronic spin and the similar quantity of the nucleus, the nuclear spin I. It also includes the effects due to the finite size of the nuclear radius. Additionally, degenerate states split into distinct levels within an external magnetic field. The overview of all the contributions can be viewed in Figure 2.1.

2.1.2 Multiple electron systems

In systems with more than one electron the Hamiltonian not only has to be expanded by the potential and kinetic terms for each electron but also by their interaction with each other.

$$\hat{H} = \sum_{i=1}^{N} \left(-\frac{\hbar^2}{2m} \Delta_i - \frac{Ze^2}{4\pi\epsilon_0 r_i} \right) + \sum_{i<j}^{N} \frac{e^2}{4\pi\epsilon_0 r_{ij}} \tag{2.4}$$

This makes the Schrödinger equation analytically unsolvable and consequently approximation models need to be used. Instead of considering all electrons simultaneously, their energy-levels are determined successively. Then, a shielding factor for the charge of the nucleus by the average spacial distribution over time of previous electrons is applied [12].

These considerations are none the less still untenable because the key principle of interactions between electrons is neglected: The Pauli principle. When describing atomic

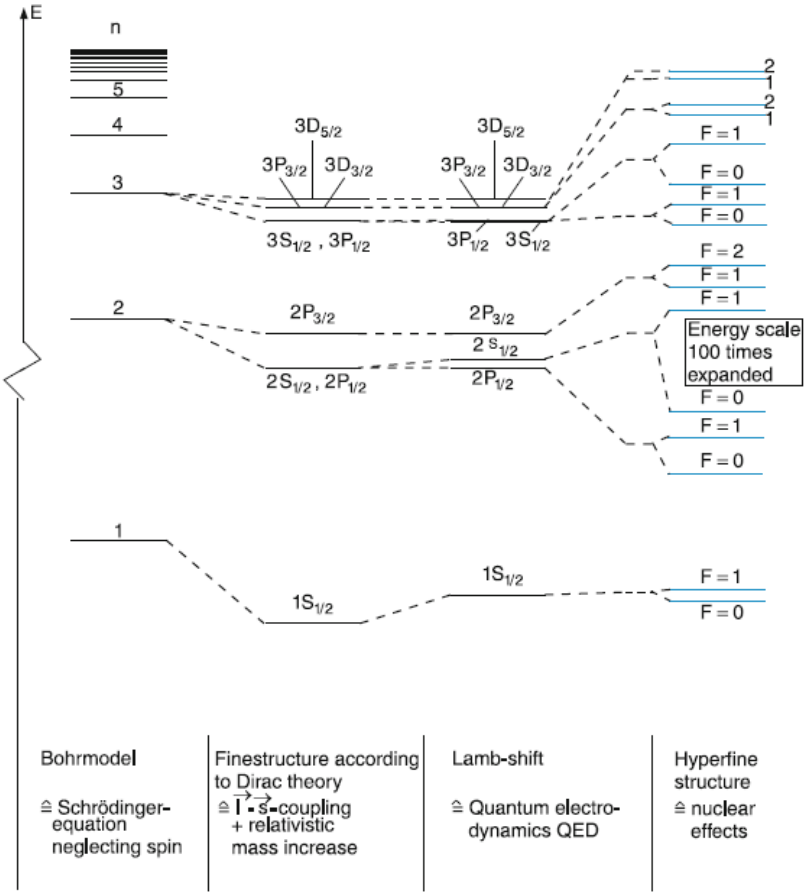

Figure 2.1: The hydrogen atom level scheme including all known effects to date. The levels are not to scale to visually magnify the splitting and shifts. Taken from [12]

states it can be formulated as the following: each atomic state determined by the quantum numbers (n, l, m_l, m_s) can be occupied by at most one electron. In the atomic shell model the structure arising from those very concepts is presented, though it does not provide the capability to calculate the many particle wave function. This is achieved for example with the Hartree-Fock method [12], which iteratively calculates the wave function from the Slater determinant.

The shell model divides the states into electron shells with respect to their principal quantum number n. Each of these shells accepts $2n^2$ electrons and is divided into subshells according to their angular momentum quantum number l (Table 2.1).

Table 2.1: Maximum number of electrons in different atomic subshells

n	1	2		3			4				5		6
Shell	K	L		M			N				O		P
Subshells	$1s$	$2s$	$2p$	$3s$	$3p$	$3d$	$4s$	$4p$	$4d$	$4f$	...	$5g$	...
Number of electrons	2	2	6	2	6	10	2	6	10	14	...	18	...

2.2 Highly charged ions

Generally, qualitative terms underlie a certain margin of interpretation. Likewise, there does not exist a strict rule, for when ions are considered highly charged ions (HCI). But in most cases single or twice charged ions do not fall into this category.

As introduced before, HCI naturally occur in the plasma of stars and other astrophysical objects but can also be produced in EBITs. The interaction processes which for example dictate the charge state distribution within the trap region, are discussed within this section.

2.2.1 Ion interactions

At first we investigate the processes between ions themselves. When ions of the same element come close to each other, the higher charged ion A^{m+} is able to capture a number x of electrons from the initially lower charged ion B^{n+}

$$A^{m+} + B^{n+} \rightarrow A^{(m-x)+} + B^{(n+x)+}.$$

This process is called **charge exchange (CX)**. As the total energy on the right hand side will usually be less than that of the left hand side, the excess energy actually results in the excitation or even ionization involved electrons. The same mechanism happens between ions of different elements, though here not the charge state but the binding energy determines the direction of the process. Since for CX the Coulomb repulsion of the ions has to be overcome by kinetic energy, the process becomes more important for higher temperatures.

2.2.2 Electron impact ionization and excitation

The most important mechanism for ionization of ions is **electron impact ionization (EII)** [12]. If an electron with sufficient kinetic energy E_{kin} hits the ion X^{q+} it has the chance to release a second electron

$$e^-(E_e) + X^{q+} \rightarrow e^-(E_1) + X^{(q+1)+} + e^-(E_2).$$

This describes EII and the ionization energy E_i can be determined through

$$E_1 + E_2 = E_e - E_i.$$

If the energy of the electron does not exceed the ionisation energy the probability to instead excite the ion into a permitted higher state rises. The process

$$e^-(E_e) + X^{q+}(n,l) \rightarrow e^-(E_e') + [X^{q+}(n',l')]^*$$

is called **electron impact excitation (EIE)**.

2.2.3 Recombination processes

Inversely, the process of **radiative recombination (RR)** is dominant for the reduction of the charge state of the ion.

$$X^{q+} + e^-(E_{\text{kin}}) \rightarrow X^{(q-1)+} + \gamma(\hbar\omega)$$

In this process an electron within the plasma is captured by an ion. A photon with the energy

$$\hbar\omega = E_{\text{kin}} - E_{\text{ion}}$$

is emitted in the process, hence the name radiative.

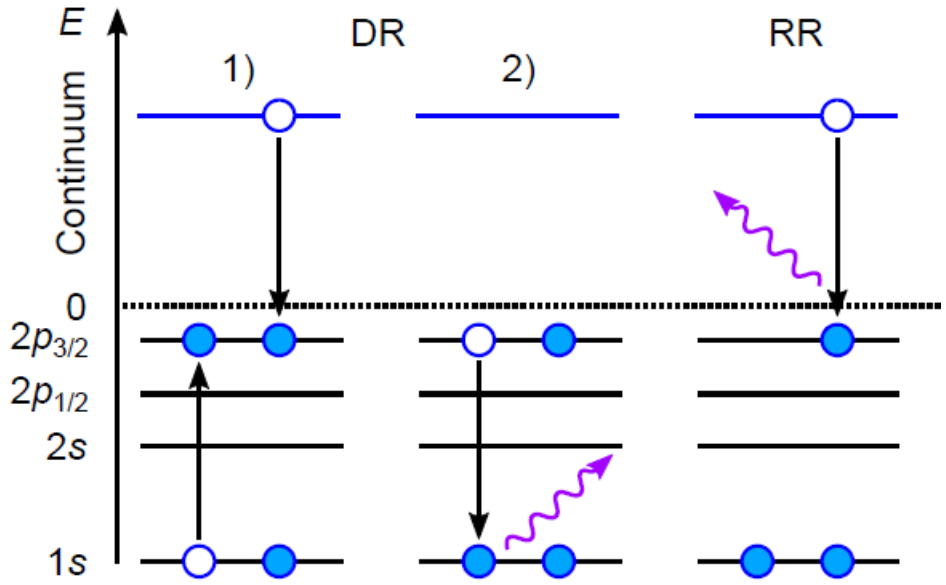

Figure 2.2: The level scheme of the radiative recombination processes. The dielectric recombination (DR) has two steps. First an electron from the continuum is captured and simultaneously an electron is lifted into a higher state. then, a photon is emitted as the ground state is reached. In the radiative recombination process the photon is emitted as the electron is captured. Changed from [13]

The other process reducing the charge state of the ions is **dielectric recombination (DR)**. An already bound electron is lifted into a higher energy level as an electron is

captured from the beam as seen in Figure 2.2. The total energy gain by capturing the electron must match the transitional energy of the electron which is raised into a higher level. From the hereby reached excited state, the ion may decay into the ground state by emitting a photon of the energy matching the transitional energy between the states.

This photon energy $E(\gamma) = \Delta E_n$ is not proportional to the beam energy, but only occurs at certain electron energies. Consequently it is called a resonant recombination. Later this property is used to calibrate the photon energies in Chapter 4. Similar mechanisms with more than two involved electrons do exist, as this exceeds the scope of the thesis, the interested reader is referred to [14].

2.3 Working principle of electron beam ion traps

An electron beam ion trap (EBIT) is a laboratory instrument for the production, storage, excitation and analysis of highly charged ions (HCI). Its first type was conceived and built in 1986 at the Lawrence Livermore National Laboratory (LLNL) by Mort Levine and Ross Marrs, as an alteration on the EBIS concept [15]. Reduction of the trapping region from nearly a meter to only a few centimeters solved the EBIS's drawback of unstable plasma and the switch to a Helmholtz coil magnet configuration enabled direct examination inside the trap. Since then, a multitude of EBITs have been constructed with various designs. Dependent on the requirements they vary in size, orientation, beam energy and also cooling method [7]. The general concepts of an EBIT is presented in the following.

2.3.1 General concept

In Figure 2.3 one can observe the general concept of an EBIT. Electrons are emitted at a cathode and accelerated towards the trap region. In the process it is magnetically compressed along the converging magnetic field lines generated by a magnet. Ions are trapped radially by the magnetic field and the electric space-charge potential of the beam. The electrostatic potential generated by the drift tubes allows to trap the ions axially. After leaving the trap region the electron beam is decelerated, diffused and captured inside the collector.

Each part mentioned above is further elaborated on and explained for the Hyper-EBIT in Chapter 3.

2.3.2 Properties of the electron beam

The main parameters of the electron beam are foremost its energy and current. On a closer look the spacial distribution of the beam and its potential are of interest to determine the effective beam energy.

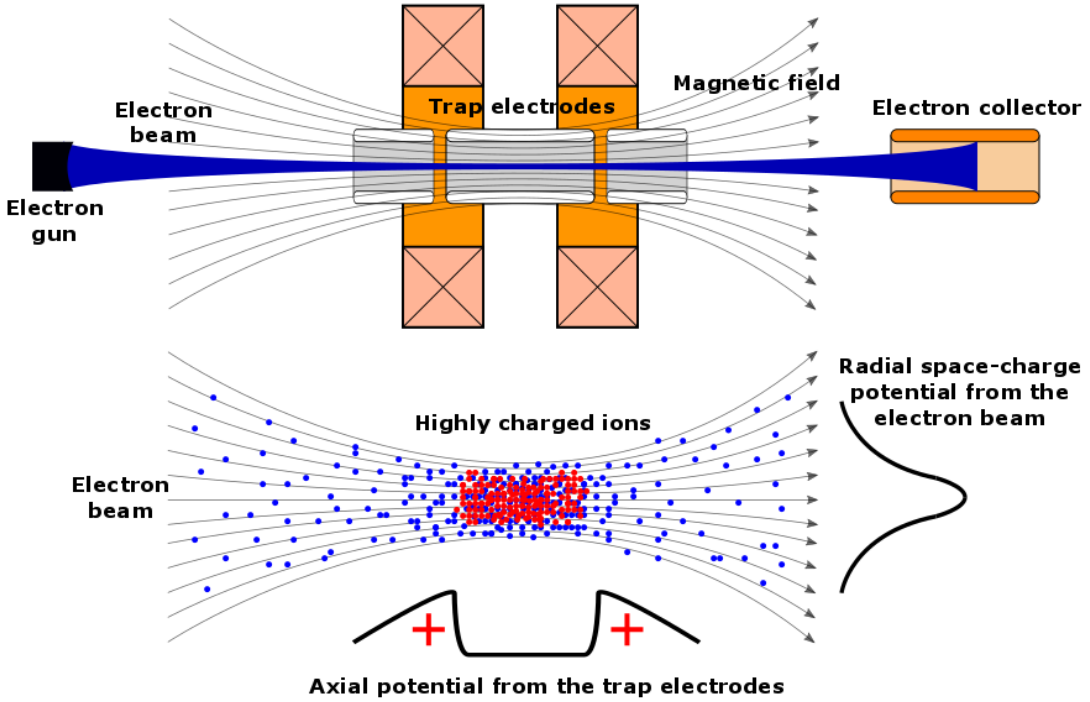

Figure 2.3: Schematic concept of an EBIT. On the top the main components with the electron beam and the magnetic field are depicted. Below the two trapping potentials for the ions are sketched. Taken from [16]

Electron beam current

The current supplied by the cathode power supply corresponds directly to the electron beam current I_b. If the beam inside the EBIT is well adjusted, losses along the beam path, due to capture at the various electrodes should be minimal. In consequence the current draining through the collector is also approximately equivalent to I_b.

Uncorrected electron beam energy

In a first approximation the energy of the electrons is determined by the potential difference between the cathode and the central trap electrode. The potential of the cathode U_{cath} is negative while the voltage applied to the central trap U_{trap} on the other hand is positive. Additionally, a negative bias voltage can be supplied to the electron gun (see Figure 3.2) so an extra term U_{bias} has to be subtracted. Therefore the uncorrected electron beam energy is given by

$$E_{\text{beam}} = e\,(U_{\text{trap}} - U_{\text{cath}} - U_{\text{bias}}). \tag{2.5}$$

The space charge of the electron beam itself will reduce the effective energy of the

electrons. In order to quantify this contribution, the spacial distribution needs to be known.

The potential of the electron beam

In order to retrieve the electron beams potential we consider the beam as a quasi-static distribution of charges. Another useful simplification is viewing the electron beam as a cylinder of radius r_0 with infinite axial extent and uniform charge density

$$\rho(r) = \begin{cases} \dfrac{I_b}{\pi r_0^2 \dot{z}} & \text{for} \quad r \leq r_0, \\ 0 & \text{else.} \end{cases} \tag{2.6}$$

The axial velocity of the electrons $\dot{z}$ can be calculated with the relativistic dispersion relation from the acceleration voltage U. As primarily the electron beam characteristics at the center of the trap are of importance it is given by Equation (2.5).

To retrieve the potential of the electron beam we make use of Poisson's equation

$$\Delta\phi = -\frac{\rho}{\epsilon_0} \tag{2.7}$$

with the Dirichlet boundary condition, which specifies the potential on the surface of the drift tubes $\phi(r_{\mathrm{dt}}) = U_{\mathrm{dt}}$. Here ϵ_0 is the vacuum permittivity, r_{dt} and U_{dt} the radius and potential of the drift tube. The resulting potential is given by the following:

$$\phi_<(r) = \phi_0 \left(2 \ln \left(\frac{r_0}{r_{\mathrm{dt}}} \right) + \frac{r^2}{r_0^2} - 1 \right) + U_{\mathrm{dt}}, \tag{2.8}$$

$$\phi_>(r) = \phi_0 \left(2 \ln \left(\frac{r}{r_{\mathrm{dt}}} \right) \right) + U_{\mathrm{dt}}. \tag{2.9}$$

In the process a the factor

$$\phi_0 = -\frac{I_b}{4\pi\epsilon_0 \dot{z}} \tag{2.10}$$

was introduced, which also indicates the energy spread inside the beam by $\phi_<(r_0) - \phi_<(0) = \phi_0$.

Furthermore, the space charge potential of the beam can be given by

$$\phi_e = \phi_0 \left(2 \ln \left(\frac{r_0}{r_{\mathrm{dt}}} \right) - 1 \right) \tag{2.11}$$

which is the potential in the center of the beam without the drift tube voltage.

Spacial distribution of the electron beam

Upon emission at the cathode the electrons perform a circular motion due to the magnetic field. As the magnetic field strength B gets stronger towards the center of the EBIT, the radius of the circular motion decreases. The previous consideration of the beam

potential yields the radial electric field through $\mathbf{E} = -\nabla\phi$. Together with the Lorentz force it must compensate the centrifugal force of the circular motion. This results in the Brillouin radius [17]

$$r_b = \sqrt{\frac{2I_b m_e}{\epsilon_0 \pi \dot{z} e B^2}}, \tag{2.12}$$

as measure for the radial extent of the beam. As the actual beam does not form a laminar flow Gabriel Herrmann made use of optical theory [18] to more thoroughly describe the resulting spacial distribution of the electron beam. He thereby accounts for the temperature of the electrons and considers the residual magnetic field at the cathode B_c.

Based on his theory the formula for the radius through which 80 % of the electrons pass [19] is

$$r_h = r_b \sqrt{\frac{1}{2} + \frac{1}{2}\sqrt{1 + 4\left(\frac{8k_B T_c r_c^2 m_e}{e^2 r_b^4 B^2} + \frac{B_c^2 r_c^4}{B^2 r_b^4}\right)}}. \tag{2.13}$$

This is the so-called Herrmann radius based on the Brillouin radius r_b from Equation (2.12). In these formula k_B is the Boltzmann constant, m_e the electron mass, the elementary charge is e, the vacuum permittivity is ϵ_0 and r_c is the radius of the cathode.

Effective electron beam energy

As mentioned before, the space charge of the electron beam contributes to the effective electron beam energy. The negatively charged electrons effectively reduce the potential difference between the central trap electrode and the cathode. This shift is partly compensated by the space charge of the built up positively charged ions in the trap.

A compensation factor

$$f = \frac{\sum_q n_q q}{n_e e} \tag{2.14}$$

with the density of electrons n_e and the density of q charged HCI n_q is introduced [20]. A precise theoretical determination of f is not possible, as it heavily depends on factors like the axial trap depth, the amount of ionizable atoms, charge breeding times and residual gas pressures. Therefore it can only be estimated through the analysis of resonant spectral lines, as demonstrated in Chapter 4.

Other things like the cathode work function, image charges in the drift tubes etc. are also shifting the beam energy, but typically contribute little to the overall beam energy. In the end we write

$$E_{\text{eff}} = E_{\text{beam}} - e\,(1 - f)\,\phi_e \tag{2.15}$$

for the effective beam energy.

2.4 Working principle of high-purity germanium detectors

Spectral analysis of HCI stored inside an EBIT naturally requires some sort of photon detection device. As usual photon energies lie inside the X-ray spectrum, high-purity germanium detectors are optimal for this application. The following sections briefly explain how such a detector works.

2.4.1 Semiconductor p-n Junction

Contrary to conductors a semiconductor presents itself by a band structure within the crystal, resulting in a band occupied by electrons called **valence band** and an empty **conduction band** above. The energy E_V lies at the upper edge of the valence band, while E_C is located at the lower edge of the conduction band, implying the **band gap** of $E_g = E_C - E_V$. This energy determines crucial electronic properties and usually amounts to a few electron volt.

By introducing impurities of other atoms into the crystal structure we get **doped** semiconductors. In the context of this crystal structure an impurity atom with a greater number of outer shell electrons is called **donator**, one with less **acceptor**. Materials doped with predominately donators are named *n-doped* because of their extra negative carriers. The absence of electrons within a crystal structure is viewed as a hole and appears to be a positive charge carrier. Crystals with extra positive carriers are named *p-doped* and primarily doped with acceptors.

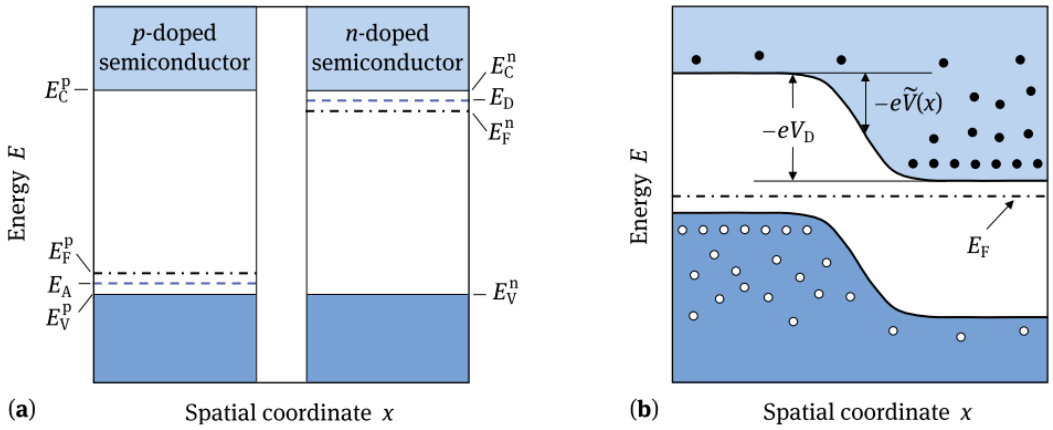

Figure 2.4: **a)** Fermi levels and the corresponding band edges for the n- and p-doped semiconductor. **b)** A p-n Junction in equilibrium. Taken from [21]

In the n-doped semiconductor, extra donor levels E_D directly under the conduction band must be taken into account. This results in a raised Fermi-level E_F^n which no longer lays in the middle between the valence and conduction band. As seen in Figure 2.4 (a) this applies inversely for acceptor levels E_A.

By combining two differently doped types of crystals a so called p-n Junction is created. The concentration gradient of negative and positive carriers induces a diffusion current across the boundary surface. Here, the *depletion zone* forms where the free holes and electrons recombine causing a region without free charge carriers. As a result the conduction and valence band form step-like and are shifted by the **diffusion voltage** $V_D \approx E_g$ [21, S.411]. This leads to a corresponding field current offsetting the diffusion current settling in an equilibrium (Figure 2.4).

2.4.2 Photon detection with HPG detectors

For photon detectors properties of the depletion zone are used. The general setup of a detector is a so-called PIN diode, basically a p-n Junction with a undoped layer between the two differently doped layers. A negative voltage applied at the p-doped side enlarges the depletion zone over the intermediate layer, which is the active volume of the detector. When a photon with sufficient energy is absorbed there, electron hole pairs are created. Due to the electric field present in this region the charge carriers are separated and can be detected as excess current. As the integrated current is proportional to the energy of the photon the latter can be measured. The principle is illustrated in Figure 2.5.

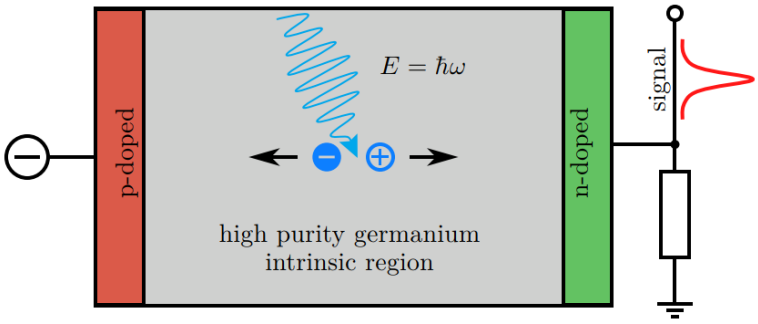

Figure 2.5: A schematic of the principle of photon detection in a PIN diode. The absorbed photon creates electron hole pairs, resulting in an integrated current proportional to the photon energy. From [22]

Germanium is a semiconductor with a high absorption coefficients for x- and γ-rays. On top it is available in very high purity which makes it an optimal choice for photon detection [23]. However, due to the relatively small band gap of 0.625 eV at room-temperature, germanium detectors suffer from large noise due to thermal excitations. In order to reduce this noise background, germanium detectors are typically cooled by liquid nitrogen to around 77 K.

3 Experimental setup and measurement processes

3.1 The Hyper-EBIT experiment

In the scope of this thesis, the previously relocated Hyper-EBIT was recommissioned. It was designed as a high voltage and high current EBIT, for the purpose of spectroscopy and HCI ejection. [20] After intervals of temporary use since its completion in 2012 it now is destined to replace the HD-EBIT.

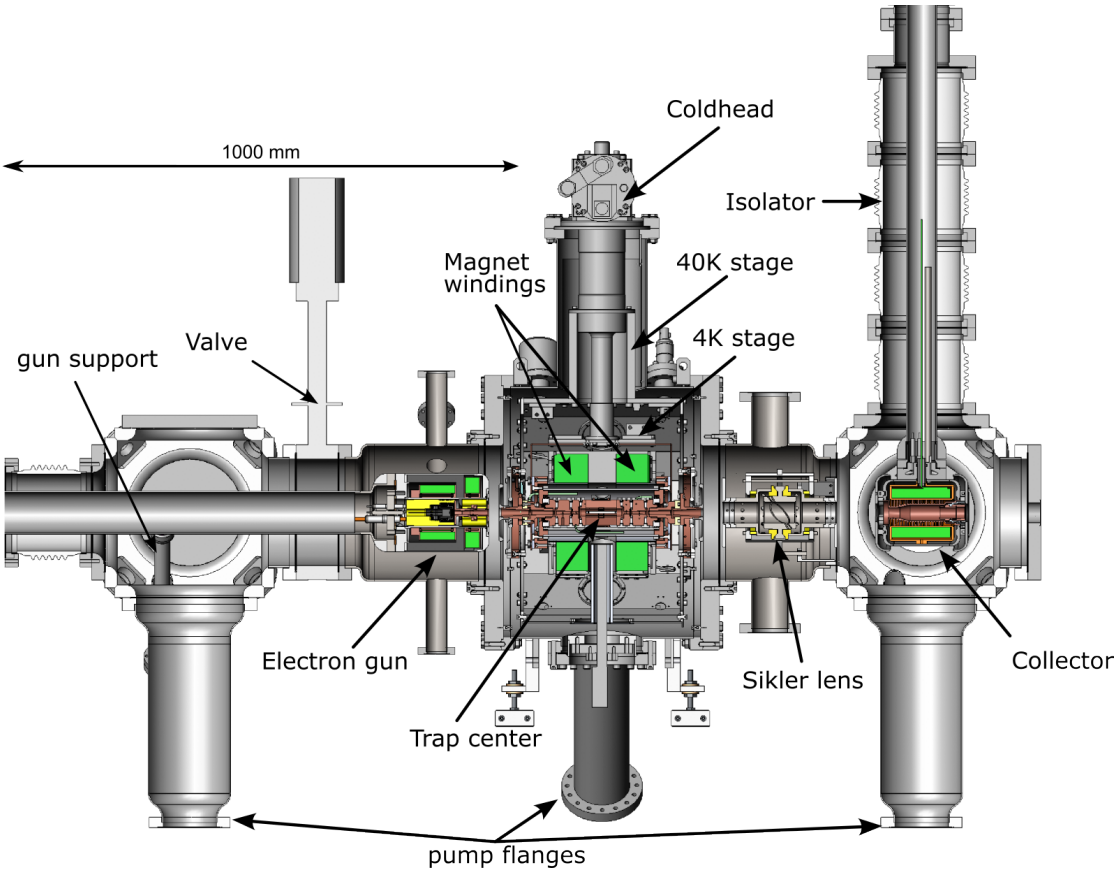

Figure 3.1: Axial cross section of the Hyper-EBIT. Adapted from [20]

Compared to the HD-EBIT the Hyper-EBIT provides larger clearance of the high-voltage components and is equipped with a cold head for cooling of the superconducting

magnet, which allows for continuous and cost-efficient operation. The axial cross sectional view of the CAD-model from 2012 (Figure 3.1) displays, that the Hyper-EBIT's electron gun and collector are isolated from ground. Therefore, if installed on a high-voltage platform, the gun and collector can be raised to voltages up to 300 kV. In total, this design aimed at the efficient production and ejection of heavy hydrogenlike ions. This section presents an overview of the different parts of the Hyper-EBIT, while the following explains the IGLET detector and the measurement process.

The whole EBIT is enclosed within an array of stainless steel sections specifically manufactured for it, forming a vacuum chamber. Turbo pumps at the main three parts

- electron gun,
- magnet,
- and collector

keep the pressure at ultra-high vacuum ranges of currently around 1×10^{-9} mbar. The necessary pre-vacuum of 1×10^{-4} mbar is provided by a powerful scroll pump in line with a single turbomolecular pump. This system is mounted inside the structural frame supporting the Hyper-EBIT from below. A hand-operated valve creates a separated compartment for the electron gun. With a large manipulator, the gun can be retracted into this section. Aided by a NEG-pump (non-evaporable getter pump) attached to this chamber, it is possible to ensure ultra-high vacuum for the electron gun during transport or in case of power shortages.

3.1.1 Electron gun

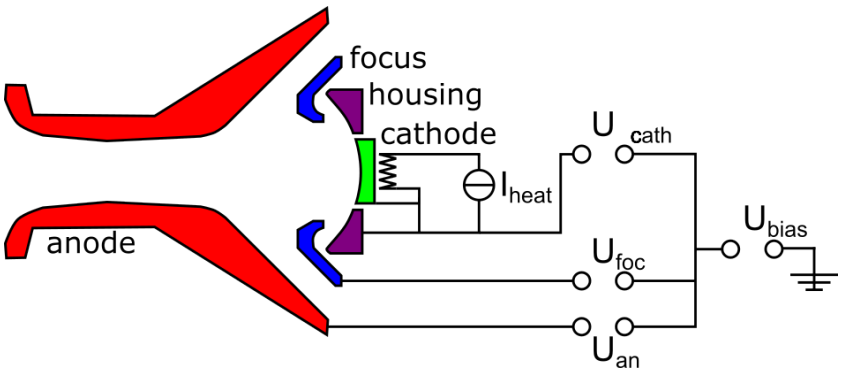

Figure 3.2: Schematic of an electron gun with circuit diagram. Adopted from [20]

The electron gun generates a beam of electrons and is therefore an integral part to the operating principle of an EBIT. Electrons are emitted from the spherically indented surface of the dispenser cathode, made out of a porous tungsten matrix mixed with a barium-based low work-function material to support thermal electron emission. More on the composition of the used cathodes can be found in [24]. By heating the cathode with

a small current through a tungsten filament to roughly 1400K, thermionic electrons are emitted. In the process, small fractions of barium atoms are also liberated from the surface and introduced into the vacuum inside the EBIT, which are substituted by diffusion from the inner reservoir. The cathode surface is very sensitive to contamination through abundant molecules in the ambient air like O_2, H_2O or CO_2. Contamination poses a significant risk to the working condition of the cathode, for why it must be kept at ultra-high vacuums at all times.

During this thesis, a cathode with a diameter of 3.4mm is installed, capable of a maximum emission current of 500 mA [1]. Required heating power is reached with a current of 1.3A through the heating filament. The installed gun is also able to accommodate a larger cathode with a diameter of up to 6.3mm, pushing the maximum emission current to 2A. A sectional view of the Hyper-EBIT's electron gun CAD model is shown in Figure 3.3 .

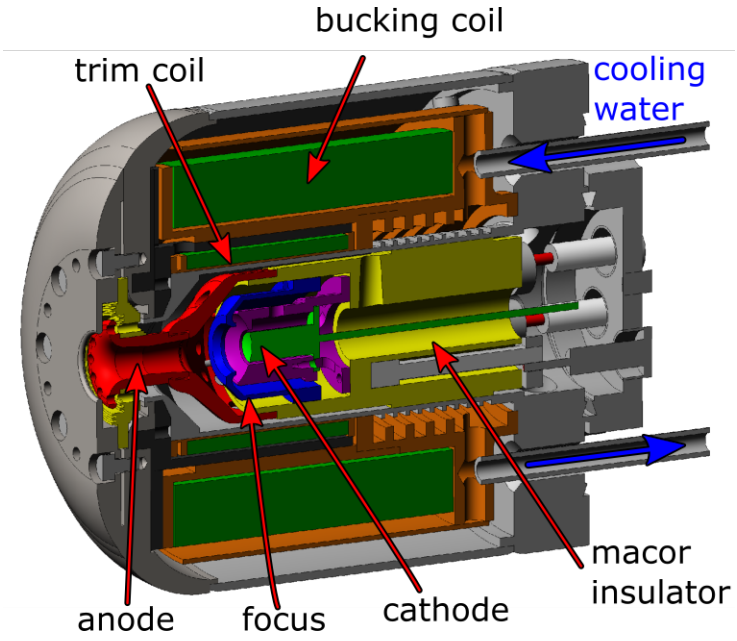

Figure 3.3: A cross sectional view of the electron gun in the Hyper-EBIT. Adapted from [20]

From the cathode the electrons are accelerated towards the copper anode and focused into a beam with the focus electrode. As the housing of the cathode follows the Pierce-geometry [25], the beam is focused naturally at the space-charge limit. Generally the focus electrode is intended to further optimise the beam characteristics. It is also used to block the electron emittance by applying a strongly more negative voltage than present at the cathode. Inversely for raising the current of the electron beam the focus is set to a positive voltage. As the focus electrode is closer to the cathode, for raising the beam

[1] The installed cathode is manufactured by *Spectra-Mat, Inc.* and has the part number 113-155 with SN: 3

current, it often is more effective to use the focus than to raise the anode potential.

In Hermann's theory the optimal compression of the electron beam is achieved, if no magnetic field is present at the cathode. The so called bucking coil wrapped around a soft iron core is intended to provide the required magnetic field. A trim coil is installed to smooth out the junction to the main magnetic field of the EBIT. Cooling water from the facility circulates around the coils transporting the generated heat away.

3.1.2 Magnet and trap

Located at the center of the EBIT is a trap. It is positioned inside the magnet which provides the strong magnetic field for compressing the electron beam. Consisting out of two Nb_3Sn superconducting coils, the Helmholtz configuration magnet was manufactured by *Cryogenic Ltd.* especially for the Hyper-EBIT. Its critical temperature $T_c(B = 0)$ lies at 18.3 K and is rated for a magnetic flux density up to 7 T.

A two stage cold head keeps the magnet below the critical temperature of the superconductor. At the first stage it reaches a temperature of 40 K with a cooling power of 31 W, while the second stage is cooled to 4.2 K. In the following they are referred to only via their temperature.

The magnet with its holder and most of the inner trap electrodes are thermally linked to the 4 K stage. Highly pure copper bands (99.997% purity) provide a optimal heat transfer to the cold head. Structurally, the whole inner assembly is hung from thin titanium spokes to limit heat influx from the outside. To help with that, a silver coated copper shield is connected to the 40 K stage, absorbing and reflecting the heat radiation from the outer chamber walls (300 K).

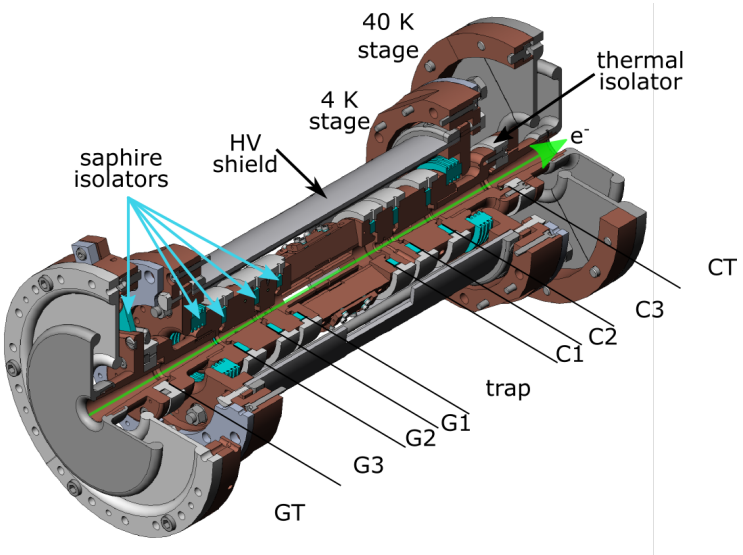

Figure 3.4: A view through the trap electrodes (the drift tube setup). Changed from [20]

The trap electrodes combined form the so-called drift tube setup, which is depicted in Figure 3.4. It features 9 individual electrodes: The 100 mm long center electrode with a diameter of 14 mm and four electrodes each at gun and collector side. Their diameter increases conically from 5 mm at the most inner electrode G1 (respectively C1) to 14 mm at the outside of GT (or CT). In total this assembly is 383 mm long.

All the inner electrodes are cooled by the 4 K stage and thermally linked with sapphire rings. This insulator provides exceptional thermal conductivity between the thermally and electrically highly conducting OFHC-copper (*oxygen-free high thermal conductivity*) electrodes. In order to guarantee a homogeneous potential their surface is coated in gold, protecting them from oxidation. The outer trumpet electrodes at the gun (GT) and collector side (CT) are cooled through the 40 K stage and are only connected to the inner electrodes by an isolator with low heat conductance.

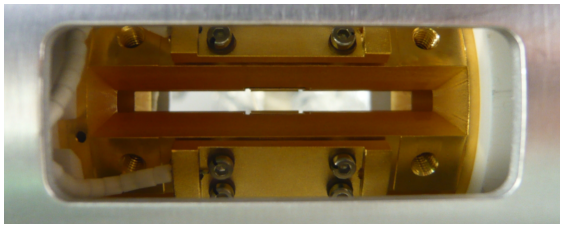

Figure 3.5: A view through one of the windows in the HV shild. The central trap electrode is visible. [20]

The central trap electrode consists of eight sections to allow for radial access to the trap. Consequently the HV shield, magnet holder and the 40 K shield feature windows in the corresponding directions. As the cold head cryocooler is installed above the trap, they do not have a top opening. On corresponding flanges on the vacuum chamber diagnostic devices or injection systems can be installed. A view through one port can be seen in Figure 3.5.

3.1.3 Ion optics

Following the direction of the beam, a Sikler lens [26] is installed after the drift tube setup (see Figure 3.1). This special electrostatic einzel lens helps to focus and manipulate the ion bunches upon extraction from the trap. Due to its four way split design it allows for orthogonal manipulation in both x and y direction. The central electrode of such lenses focusses the beam by applying a positive bias, while the other electrodes act as deflection plates. As no ions were extracted in the scope of this thesis, it is referred to [20] for more detail.

3.1.4 Collector

Completing the basic setup of an EBIT, the electron beam is defocused and captured in the collector. When electrons at about $eU_{\mathrm{cath}} = 4$ keV reach the collector with a current

of 1 A, a power of 4 kW of heat must be dissipated. Similar, to the electron gun, cooling water is running trough the collector, carrying away the dissipating heat.

In Figure 3.6 a cross-section of the collector is depicted. Centrally, the large collector electrode from OFHC-copper features fins on the outside, which the cooling water flows around. Enlarging the surface and improving the spread and transmission of the generated heat. A magnet coil offsets the fringe field of the superconducting magnet to strongly defocus the electron beam. This collector coil is also cooled by the water flow and can be operated at a maximum current of 30 A resulting in a magnetic field of 120 mT.

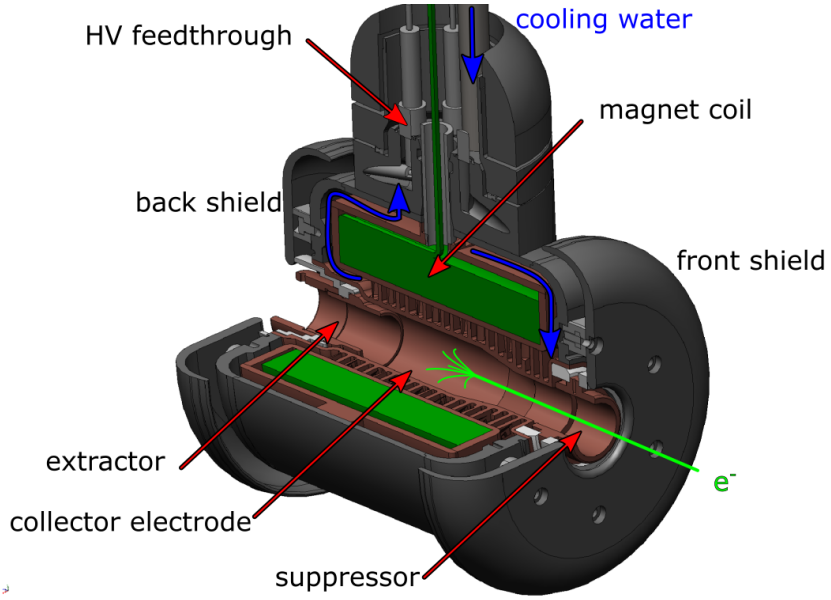

Figure 3.6: A sectional view of the CAD model of the electron collector of the HyperEBIT. Adopted from [20]

The suppressor electrode at the front of the collector guides the electron beam and incoming ions into the collector. Moreover it provides a measure for the alignment of the beam. By reducing the current which results from the beam hitting the suppressor, the EBIT's operation parameters are optimised. For blocking the electrons the extractor is placed at the end of the collector. Set to a higher negative voltage than the cathode U_{cath} it prevents the electrons from passing through. Similar to the suppressor it is also intended to guide ions in the extraction process.

Two steel shields are installed at the front and back side of the collector to improve the field properties. The rearward opening allows the ejection of ion bunches, when the EBIT is used as an ion source.

3.1.5 Gas injection system

Not part of the EBIT's core setup but essential for its operation is an injection system for the target material. In Figure 3.7 the implemented gas injection system is depicted.

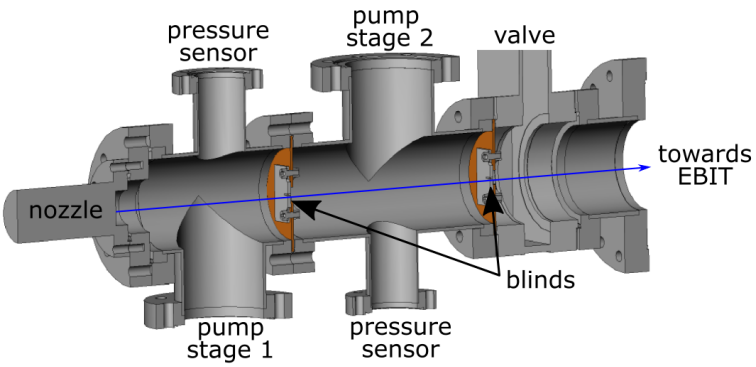

Figure 3.7: The gas injection system with its two stages separated by blinds. Changed from [20]

This system consists out of a nozzle and a two stage pump system, each followed by a collimator with 1×10 mm slits. Both stages are fitted with a pressure sensor so the amount of gas introduced can be adjusted with the needle valve, which is connected to the nozzle. Separated by a pressure operated valve, this contraption sits at the top right diagonal port of the trap chamber when viewed from the gun. On the 40 K and 4 K stage additional slotted covers are installed. Therefore introduced gas fills the trap volume through a directed particle stream with little contamination of the trap vacuum.

3.1.6 IGLET detector

As photon detection device an IGLET detector has been chosen. Its working principle has been explained in Section 2.4.

The IGLET detector is placed at the left horizontal port to the trap chamber if viewed from the gun. It was built by *Detector Systems GmbH* while the germanium detector and the preamplifiers themselvs were manufactured by *Ortec*. A 7.5 L liquid nitrogen dewar is directly mounted to the back of the detector resulting in usual standing times of around 5 days. Together with its electronics this is mounted on a manipulator. With it the absorption rate can be adjusted by changing the distance to the center of the trap.

To allow a wide range of operation distances a special insert for the 40 K shield of the Hyper EBIT has been manufactured in the scope of this thesis (more on that in Chapter 4). This insert features a Be foil of 25 µm thickness as boundary between the 40 K and 4 K stages. For X-rays above 1 kV, which are of interest in this thesis, beryllium is virtually transparent due to its low atomic number.

The IGLET detector is inserted into the EBIT's vacuum, but the inside of the detector, including the 1cm3 active detection volume, has its own vacuum enclosure that is separated by a second beryllium foil (see Figure 3.8). An energy resolution of down to around 150 eV is reached at photon energies of 6 keV [27]. A negative bias of −1keV is supplied to the detector when in operation.

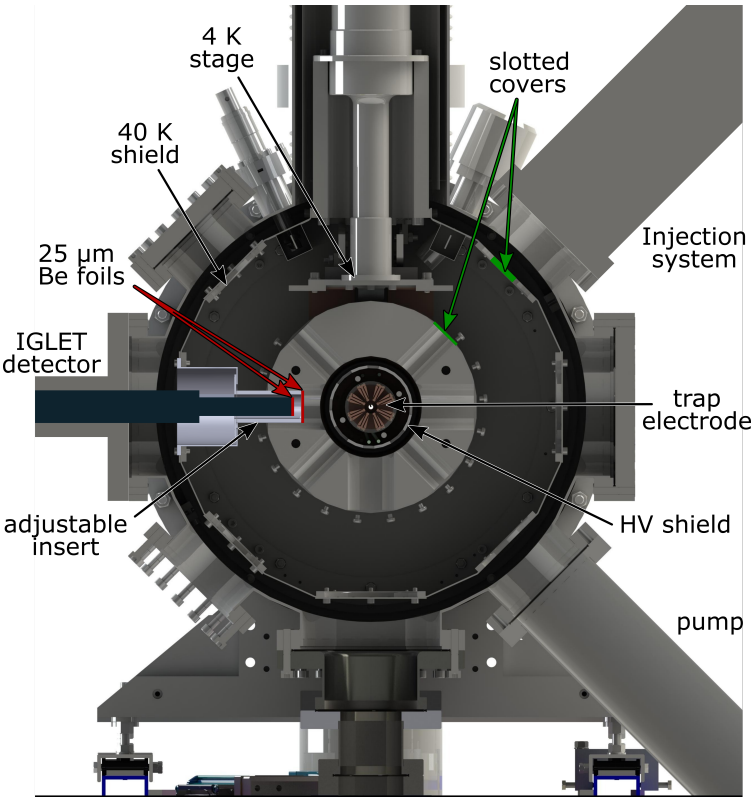

Figure 3.8: A vertical cut through the EBIT at the position of the central trap electrode.

3.2 Measurement process

To demonstrate the basic capabilities of the restarted Hyper-EBIT the spectroscopy of highly charged argon is carried out in this thesis. In more detail the resonant dielectric recombination of Ar is studied to get information about the space charge compensation due to ions and the beam. In the following the measurement process and the basic parameters of the measurements are presented.

3.2.1 Data acquisition

The photon signal from the internal preamp of the IGLET is sent to an *Ortec 672 Spectroscopy Amplifier*. From the unipolar output the amplified and now Gaussian shaped

pulse [28] is fed into one input of a *Dual Timing ADC Model 7072T* module. This analog-to-digital converter (ADC) from *FAST ComTech* performs a Pulse Height Analysis (PHA) of this signal. In coincidence to each photon signal, the voltage U_{ramp} is recorded by Sampled Voltage Analysis (SVA) at the second input of the ADC. U_{ramp} is controlled by one of the output channels of the LABBOX (more on it in Section 4.1) and indicates the present electron beam energy. Hence a 2D-spectrum can be recorded by a PC connected via a Multiparameter System (MPA).

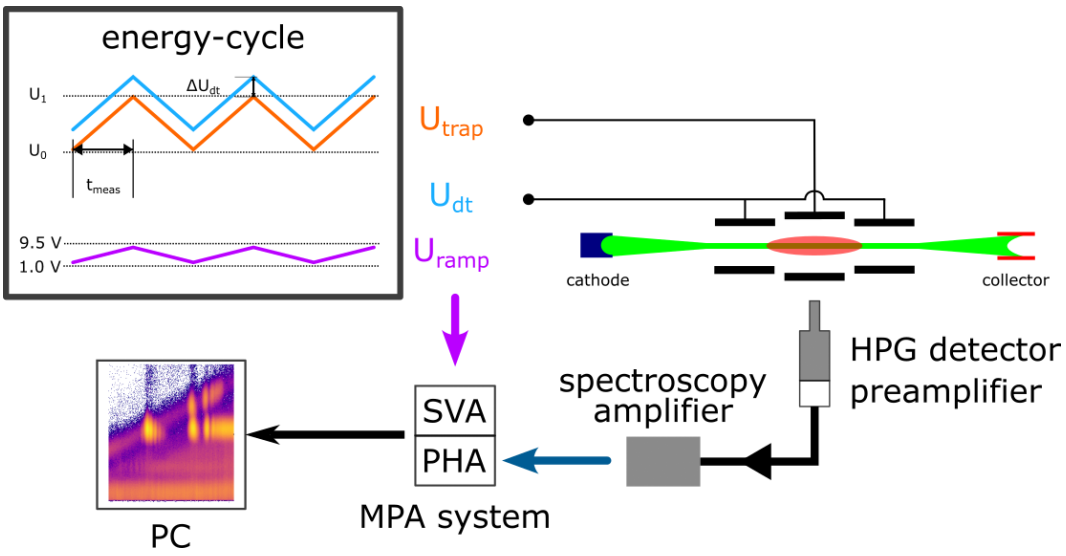

Figure 3.9: Principle of a measurement for the resonant recombination. The voltage of the central trap electrode is ramped up and down between the two voltages U_0 andU_1. To maintain a constant trap depth the drift tube electrodes are equally ramped at an offset. Photons are captured in the detector, amplified and then sent to the MPA system. The voltage U_{ramp} provides the MPA system with a measure for the applied trap voltage. Combined with the photon signals a 2D spectrum can be generated.

The schematic execution of a measurement is depicted in Figure 3.9. In order to collect data for all the resonant energies of the Argon KLL recombination at once, the trap voltage U_{trap} is ramped over a defined energy interval. As U_0 and U_1 represent the lower and upper limit of this interval, the voltage supplied to the SHA module of the MPA system is given by:

$$U_{\text{ramp}} = \frac{U_{\text{cath}} - U_0}{U_1 - U_0} \cdot 8.5\,\text{V} + 1\,\text{V}. \tag{3.1}$$

The trap voltage directly alters the electron beam energy, while the potential at the cathode U_{cath} can be kept constant. Consequently, the electric current emitted stays stable under changing electron beam energies.

The axial trap depth is defined by ΔU_{DT1}, the difference between the voltages applied to the trap and neighbouring drift tube electrodes (G1 & C1). As this defines the axial

potential of the ions, the amount and charge state distribution of trapped ions is tied to it. In consequence the ions space charge would constantly be changed, if only the central trap electrodes potential is ramped. Therefore the trap depth is kept constant, by equally ramping all drift tube electrodes at a constant offset.

Over the course of the energy ramp the voltages of the drift tube are adjusted every 500 ms. The whole voltage difference is covered in $t_{\mathrm{meas}} = 1024$ s. This limits the speed of the ramp to around 1 V/s for a good energy resolution. By ramping both up and down in sequence, a harsh voltage drop at the end of a ramp is prevented. A shift of the energy due to the direction proves to be insignificant [20].

Barium ions emitted at the cathode will slowly build up in the trap and displace the lighter Ar ions. To prevent this, the trap has to be emptied regularly. For the so-called dump, the trap electrode is raised by $\Delta U_{\mathrm{dump}} = 1000$ V. After $t_{\mathrm{dump}} = 200$ ms the trap is reset to the voltage before the dump. This time is more than enough for all the ions to be ejected. By waiting for $t_{\mathrm{wait}} = 5$ s with these settings, the charge distribution surely restores to the previous without Ba ions, completing the dump cycle. The scheme for a dump cycle can be seen in Figure 3.10.

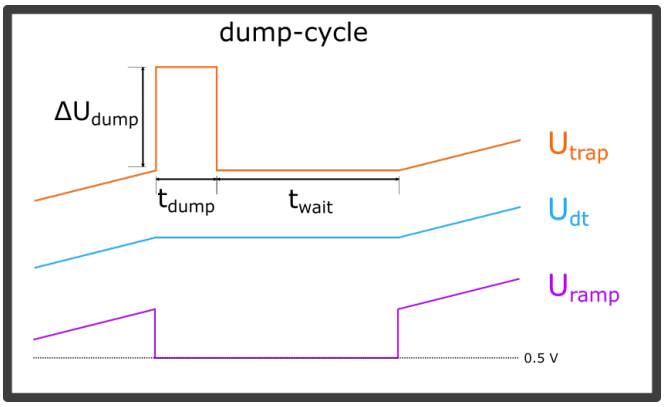

Figure 3.10: Scheme of the dump-cycle. The central electrode is raised by ΔU_{trap} to eject the stored ions. Photon events during the dump are separated by setting U_{ramp} to 0.5 V.

Throughout the whole measuring series the dump is performed randomly between every 14 s to 42 s. Over the total time of one measurement ($>$ 2 hours) this ensures an equal distribution of dumps throughout the ramped energies. While the dump is performed the voltage indicating the electron beam energy U_{ramp} is set to 0.5 V. All photons detected during any dump are hereby mapped to a separate channel by the MPA system. Upon data processing this channel is disregarded, more on that in Section 4.2.

3.2.2 Measurement parameters

By adjusting the needle valve at the gas injection system the inlet pressure was set to around 1×10^{-8} mbar to 1×10^{-7} mbar. This ensures a constant supply of Argon gas into the trap, and provides a well-defined charge state distribution in the trap.

Table 3.1: The parameters for the energy-cycle in the different measurements series

measurement	75 mA	20, 40, 60 mA
U_{cath}	-1000 V	-1000 V
U_0	+1000 V	+1000 V
U_1	+2500 V	+2000 V
ΔU_{DT1}	+50 V	+10 V
ΔU_{DT2}	-300 V	-300 V
$\Delta U_{\mathrm{DT3\ \&\ trumpet}}$	-400 V	-400 V

For the measurement, the magnet originally was ramped to 5.7 T. By the time the final set of data could be retrieved, the magnetic field measured on the outside had dropped from 165.2 mT to 134.7 mT in the two months. Assuming an analogous scaling, the field in the trap center at the end of the measurement campaign can be estimated to be ≈ 4.6 T.

The parameters of the gun and collector electrodes are optimised to accommodate a stable operation with up to 120 mA of electron beam current. For the different datasets, the beam current is varied from 20 mA to 75 mA mainly by adjusting the focus voltage while the cathode is kept at a constant voltage $U_{\mathrm{cath}} = 1000$ V.

4 Commissioning and measurements

4.1 Commissioning of the Hyper-EBIT

At the beginning of my thesis, the main objective was to demonstrate the operation of the Hyper-EBIT. Since its move into the specially built housing inside the experimental hall of the MPIK, only the vacuum system, cold head and magnet were put into operation. As first task two pressure sensors had to be replaced. Simultaneously this allowed me to have a close look at the inner components of the Hyper-EBIT in preparation of the following tasks.

To improve the temperature shielding, the slotted panels on the 4 K and 40 K shield to the unused ports were covered with a new set of closed ones. Unfortunately they could not be manufactured out of the silver coated copper, which would provide sightly better reflection of heat radiation combined with the good thermal conductance of copper. Instead polished aluminum needed to be used, as it was quickly available. Therefore the intended improvement in temperature shielding is compromised. Next, the installation of the IGLET detector was prepared.

A cylindrical cup with an adjustable second smaller diameter section was installed on the port the detector later was fitted to. As the center of the 40 K shield is shifted compared to those of the chamber flange and the magnet holder opening at 4 K (see Figure 4.1a), the inlet was designed to be adjustable. With four screws the insert can be shifted by about 6 mm right and left. As the cup itself is mounted with six equally spaced screws, a total of 6 different directions of adjustment (0, 30°, 60°, 90° 120° and 150°) are realised. In combination this guarantees the most amount of freedom in the positioning of the detector with regard to distance from the trap. A Beryllium foil is installed on the front of this cup to reduce heat radiation from the outside, while allowing the detection of x-ray photons. Before the detector could finally be installed, a support plate had to be mounted to the support frame of the EBIT.

After the flanges were closed and sealed the vacuum could be restored. Additionally the cooling water hoses were connected to the tubes running through the collector and the electron gun. In the next step a control system for the Hyper-EBIT had to be installed.

The control system is a network of EPICS servers converging on a main control PC. One monitors the temperature sensors, another one the pressure sensors and a last one controls the power supplies.

Latter is the so-called hardware-server which connects to a multichannel digital to to analog DC converter. The power supplies (PS) are connected to this so called LABBOX (*National Instruments* PCI expansion card). On its input side the analog monitoring outputs of the PS are connected. Inversely the outputs channels of the LABBOX feed a

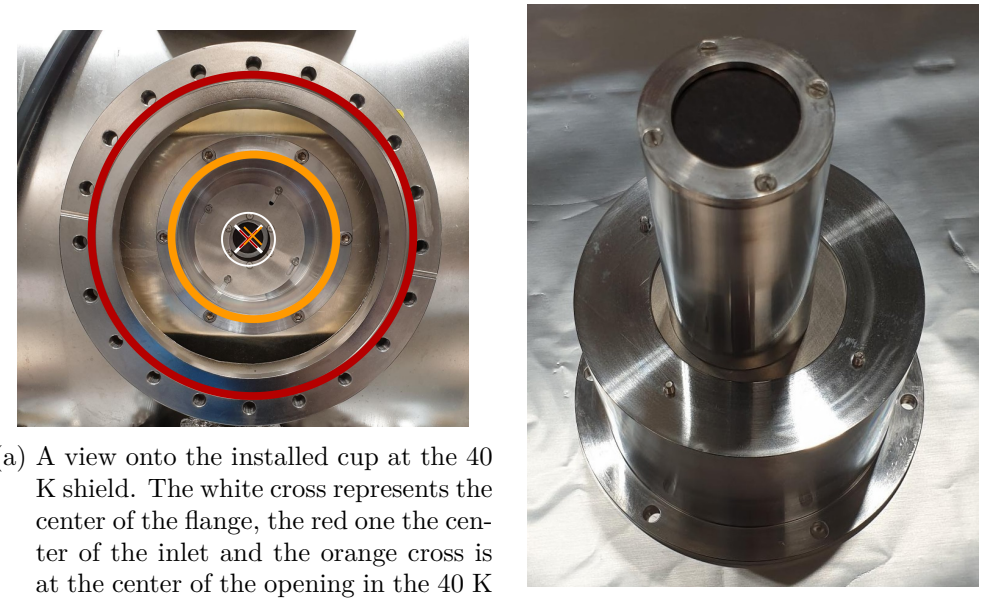

(a) A view onto the installed cup at the 40 K shield. The white cross represents the center of the flange, the red one the center of the inlet and the orange cross is at the center of the opening in the 40 K shield. With the four screws, the inlet is adjustable to compensate the offset.

(b) The cup before installation with the adjustable insert and the Be foil.

Figure 4.1: The cup at the 40 K shield for the IGLET detector.

voltage to the analog PS control inputs. The LABBOXs analog channels have a range of -10 V to 10 V. Each PS maps its output range (e.g. 0 to 5000 V) onto a subset of this interval (e.g. 0 to 5 V). So to set every voltage correctly a conversion factor has to be implemented for each PS. The hardware-server is configured to accommodate for that.

After this implementation all the power supplies were tested within the low-voltage range when not connected to the EBIT. In more detail the drift tube power supply was measured with a multimeter to quantify its deviation from the set voltage. The deviation appeared to be a gain error of about 0.5%, which resulted in a -4 V offset at 950 V. As this error only results in a lower voltage than what the PS is set to, it can be treated like a known offset with an uncertainty of about 5 V. Similarly, the cathodes PS had a gain error 0.5%, delivering always less absolute voltage. As the cathode voltage could be measured at 900 V only 100 V off its operating voltage we can assume its offset to be $(+5 \pm 1)$V. These assumptions neglect the deviations introduced by the connections to and from the electrodes themselves.

For intuitive usability a graphic user interface (GUI) for the control parameters had to be designed. The electron gun and the collector were implemented into one GUI while the drift tube setup is controlled with its own GUI (Figure 4.2).

In the setup of this thesis, the drift tube electrodes are not only connected symmetrically to the center but also the most outer electrodes (GT, G3, C3 and CT) are connected to the same power supply. Therefore, only 4 voltages for the whole drift tube setup had to be controlled, saving on PS and more importantly output channels of the LABBOX. Three HV splitters were made to allow for this configuration.

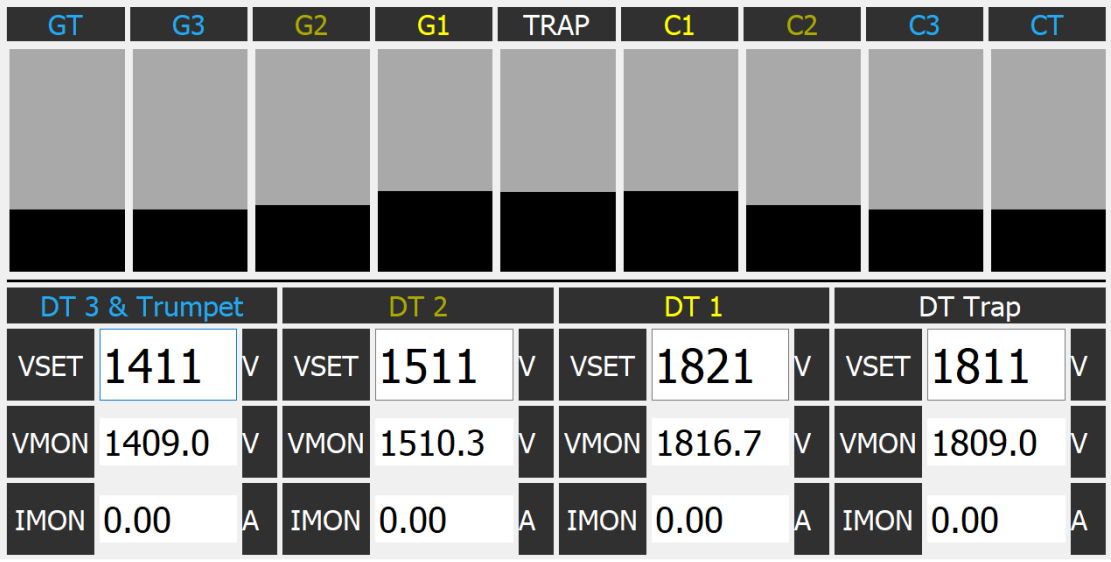

Figure 4.2: Screenshot of the drift tube GUI in operation.

With the PS connected to the EBIT a first attempt of producing an electron beam was conducted. As the gun chamber was kept under vacuum during the relocation, the cathode was not exposed to air or other forms of contamination. Consequently during cathode heating, the pressure at the gun only experienced a minor temporary increase by about half an order of magnitude. The extractor however proved to be broken, showing a significant short to ground. In result, the applicable voltage was limited by the current output of the extractors PS. Further the resistance to ground was not stable.

As the extractor is a vital component to prevent the electron beam from hitting the back chamber wall, the search for a fix had a high priority. Upon visual inspection with an endoscope a small amount of water could be spotted on the top of the collector (at the feed-throughs of the electrodes). The origin of this water can be speculated about. Most likely it is built up condensation on the metal cooling water pipes. Lacking climate control in the Hyper-EBIT housing lead to an increased humidity during the hot summer days. This benefits condensation on the 16°C cold water pipes.

The water could be efficiently removed with aided evaporation, by blowing air into the top of the collector. Further condensation would also be limited by the constant stream of relatively dry air around the cooling water pipes. Since then no excess water could be spotted again, but this did not fix the extractor.

Venting and disassembly of the collector before reinstallation would be beyond the time frame of this thesis. In any case, the collector would have to be removed later, in order to install a gas tank around it, to prevent discharge over the air when operating at 300 kV. Instead the backshield was set to a voltage of -5 kV to compensate for its suboptimal field penetration when compared to the extractor. This way, the focus voltage could slowly be raised to generate an electron beam. The pressure at the collector rose up by two orders of magnitude upon electron emission, indicating that a considerable portion

of electrons hit the back chamber wall. Using the collector coil to allow the beam to better defocus this was reduced significantly.

Sometimes the extractor would gather charge, which allowed the cathode to be set as high as -2000 V. Like this the maximum beam current of 120 mA was achieved and beam energies of 6-7 keV demonstrated. Usually while optimising the parameters of the EBIT, the extractor would rapidly discharge. In consequence the electron beam would no longer be blocked and the pressure at the collector would shoot up. To protect the EBIT the beam would quickly be blocked with the focus.

The steady and safe operation of the EBIT, despite the broken extractor, could only be assured with a cathode voltage of -1000 V. To improve beam currents on the collector and minimize the current to the anode and suppressor, the gun position was tuned. With these steps performed, the first goal of the thesis, getting the Hyper-EBIT running was completed.

4.2 Argon resonant recombination spectrum

The following section reviews the recorded spectrum of dielectric recombination of the He- to O-like (Ar^{16+} to Ar^{10+}) argon ions. Data presented in the following was recorded as described in Section 3.2.1.

The MPA system generates a text file containing information about the counts detected for given photon and beam energy. This information is given in units of ADC channels. The detector signal is mapped onto 1024 channels and the energy ramp signal to 2048.

Now a first 2D representation external of the MPA system can be generated. This is used to set parameters for the next step: A basic calibration of the x and y axis. On the x axis the interval of the energy-cycle is matched with the interval of channels which contains any counts. The channel corresponding to counts during the dump cycle is excluded in this process.

To calibrate the photon energy the $1s2p \rightarrow 1s^2$ transitional energy of helium-like Argon of ≈ 3110 eV [29] was used. A simple Gauss function was fitted to the y region of the $n = 2 \rightarrow 1$ transition in order to receive the corresponding channel.

An overview of the recorded spectra can be viewed in Figure 4.3. The prominent peaks from 2350 V to 2750 V are the KLL recombination of He- to O-like (Ar^{16+} to Ar^{10+}) argon ions. In this process an electron is captured in the L-shell ($n = 2$) while an electron from the K-shell is transitions into the L-shell. The different energy levels for every charge state result in different resonance energies. This leads to the recognizable splitting of the KLL DR resonance into multiple peaks.

At higher beam energies, the KLM-resonance can be found at about 3 kV. This resonance consists out of two different but energetically equivalent ways. An electron can be captured into the $n = 2$ level, exciting a bound electron from $n = 1 \rightarrow 3$ in the process or the electron is captured into the $n = 3$ level, inducing a $n = 1 \rightarrow 2$ transition of a K-shell electron.

The resulting intermediate state has multiple decay paths. If the electron from the

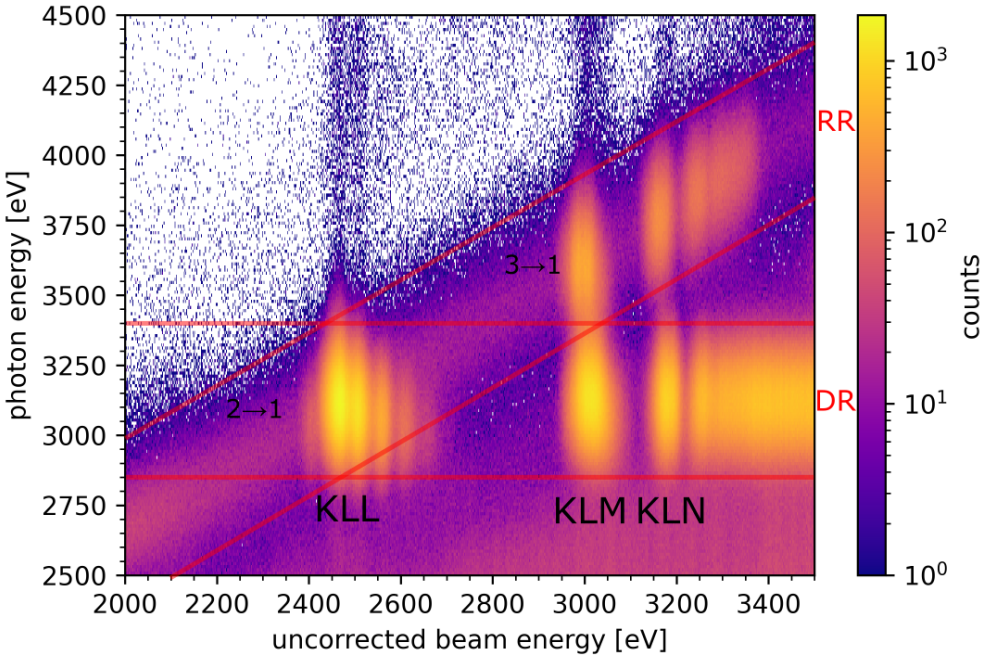

Figure 4.3: An overview spectrum of the resonant recombinations in He- to O-like argon ions across a wide energy range at 75 mA beam current.

L-shell fills the vacancy in the K-shell, a photon with the energy of the $n = 2 \rightarrow 1$ transition $E_\gamma \approx 3110$ eV is emitted. The higher peak of the spectrum at $E_\gamma \approx 3600$ eV originates from the M-shell electron radiatively transitioning into the $n = 1$ state. As intermediate step the transition $n = 3 \rightarrow 2$ also occurs, but the emitted photons can not be detected with our setup, because their energy is only about $E_\gamma \approx 490$ eV.

Similar peaks result from the KLN recombination and higher involved shells ($n = 5, 6, \dots$). Here the upper peaks are caused by the transition from the top involved shell into the K-shell.

This concludes the DR processes of argon visible in the spectrum. The horizontal region labeled with DR, contains the $n = 2 \rightarrow 1$ transitions of the argon ions and therefore not only resonant events. At an uncorrected beam energy of about 3350 eV, the electrons have sufficient energy to excite a K-shell electron into the L-shell on impact.

In the diagonal RR region, the background to the resonances originates from the radiative recombination into the L-shell. As the energy of the photons is proportional to that of the recombining electrons, the diagonally ascending pattern forms. In the following the focus of the analysis lies on the KLL DR region.

4.3 Electron beam energy calibration

Characteristic for the spectral analysis in EBIT's is the energy shift due to the space charge of the electron beam and the ions. For higher beam currents the effective energy of the electron beam decreases (see Equation (2.15)) and peaks of the resonant DR appear at higher beam energies. This effect is sightly compensated by the ions space charge, which is mainly dictated by the trap depth but linked to the electron beam.

Even in the overview spectrum in Figure 4.3 the distinct pattern of the KLL DR spectrum is visible. The first peak emanates form the dielectric recombination into argon with an isoelectronic sequence of helium. More precisely the emitted photons correspond to the $1s2s^2 - 1s^22p$ transition, consisting out of two distinct transitions of the fine structure states ${}^2P_{1/2,\,3/2}$. These transition with a photon energy of $(3044.2 \pm 0.2)\,\mathrm{eV}$ or $(3047.4 \pm 0.2)\,\mathrm{eV}$ [30] appear lower than the next prominent peak. It consists out of a multitude of overlapping KLL resonances of helium- and lithiumlike argon. In the following we will label it as the Li-like peak. Going to states of lower charge, the resonant energies appear roughly every 40 eV [31] while the photon energy decreases. As the first peak, due to its clear separation, is surely assigned to the right transition, it can be used to determine the total shift of the uncorrected beam energy.

The value of this resonance was previously determined in [32] to $(2159.7 \pm 1.1)\,\mathrm{eV}$. From the measurement at 75 mA, visible in the overview (4.3), a Gaussian fit to this peak found a energy of $(2410 \pm 25)\,\mathrm{eV}$ (Table 5.1) which yields a total shift of

$$E_{\mathrm{eff}} - E_{\mathrm{beam}} = (-251 \pm 25)\,\mathrm{eV}.$$

One must also consider the deviation of the cathode and central trap electrode voltage given in the previous section, which indicates a sightly lower shift. For the Hyper-EBIT a value for comparison could be taken from a measurement with silicon conducted in 2012 ([20]), which determined a total shift of $(-143.3 \pm 5.1)\,\mathrm{eV}$. At the least magnitude of the shift determined by this work does not seem unlikely, but the validity of this comparison must be taken cautiously. Since the main parameters influencing the space charge were different[1] to those applied here, this does not provide a solid comparison. The comparison the shift of -47 eV of the CANREB-EBIT ([33]) is also flawed, as their larger cathode diameter directly causes a lower shift as seen in Equations (2.13) and (2.15).

Nonetheless the determined value would indicate an unlikely high compression of the electron beam. By measuring the voltage at both the central trap electrode and the cathode with a precise voltage divider during the operation, could help to understand this better.

Instead of determining the total shift at one given current, the space charge contribution due to the electron beam can be determined by comparing the relative shifts between measurements at various beam currents. Therefore four measurements with beam currents between 20 mA and 75 mA have been recorded in the KLL DR region. On the search for the optimal parameters for the energy- and dump-cycle the trap depth was

[1] $E_{\mathrm{beam}} = 1.5$ keV, $I \approx 40$ mA, trap depth ≈ 50 V and lower charged ions.

changed for the 75 mA measurement (see Table 3.1). Planned measurements at lower currents with the same trap depth could not be conducted due a the sudden failure of the IGLET detector. Variation of the trap depth for the 75mA current could likewise not be recorded, which would enable the determination of the space charge contribution due to the ions. Nonetheless, the data sets for 20 mA, 40 mA and 60 mA can be analysed to determine the space charge contribution due to the electron beam.

To optimise the data collection the distance of the detector to the trap center was adjusted for each measurement. This ensured not only a sufficient rate of photons hitting the detector but more importantly limited the dead time of the PHA module to less than 5 %. Dead time is the ratio of processing and free time of the PHA.

To extract the lines from the data, all the counts in the region of interest (ROI) are projected onto the x axis. The ROI was set between beam energies of $E_{\text{beam}} = 2300$ eV and 2800 eV and photon energies of $E_\gamma = 2850$ eV to 2350 eV. A multiple Gaussian function with a constant y-axis offset $y0$

$$f(E) = y0 + \sum_{i=1}^{N} h_i \cdot \exp\left(\frac{(E - E_i)^2}{2w_i^2}\right) \tag{4.1}$$

is fitted to the resulting curve with a least square fit. Here, N is the number of gauss peaks, with central energies E_i, amplitudes h_i and widths w_i.

For lower currents the energy distribution of the electrons in the beam determined by Equation (2.10) decreases. Also the radial potential for the trapped ions decreases, further harmonizing the temperature distribution of them. Both of these effects result in a higher energy resolution at lower beam currents. Consequently a total of 10 peaks could be fitted to the 20 mA data, including a line for O-like Ar. Because the charge state distribution shifts to lower charged ions, for lower beam currents, the Ar^{14+} KLL dielectric recombination is the dominant peak in the 20 mA spectrum. Some of peaks visible in the spectrum are the result of overlapping resonances, which can be found in [31]. Therefore the peak of the Be-like argon is fitted with three individual lines. Similarly, for the DR resonance energy of argon with a nitrogen isoelectronic sequence two distinct peaks were fitted in the 20 mA spectrum. The region of interest with its projection onto the x axis and fit is given in Figure 4.4.

For the measurements at 40 mA and 60 mA (see Section 5.2) only six single peaks of He- to N-like argon (Ar^{16+}, ..., Ar^{11+}) could be resolved and fitted. The results of the fits with statistical uncertainties is given in Section 5.2. Their relative shift compared to the peaks at 20 mA is given in Figure 4.5. The slope of the resulting linear fit provides the quantitative measure for the total contribution of the space charge of the beam and the ions to the effective beam energy. It results to

$$\Delta V_e = (2.4 \pm 0.2)\frac{\text{V}}{\text{mA}},$$

where the error is only statistically. EBITs of similar construction, like the CANREB-EBIT have a compensations of around less than 2 V/mA [22]. The stronger compensation could indicate a stronger compression of the electron beam or are more likely

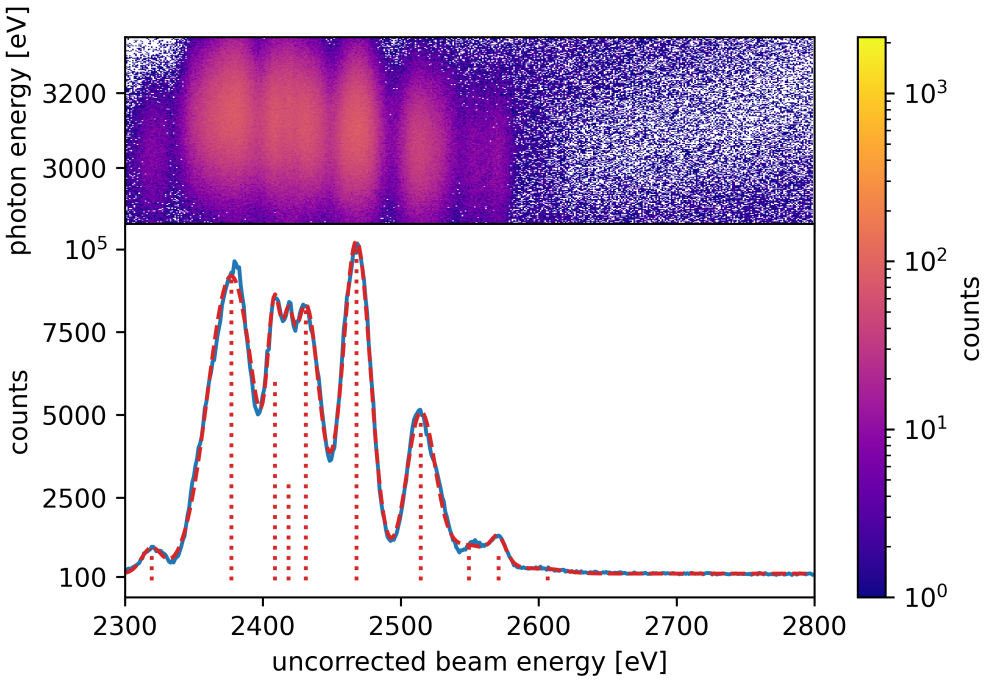

Figure 4.4: The spectrum of the KLL DR region for a beam current of 20 mA. A multi Gaussian fit is superimposed to the data. The vertical lines symbolise the extracted peak position and heights.

due to unaccounted systematic shifts. For example the potential of the drift tubes was not measured directly. By connecting precise voltage dividers in parallel to the drift tube electrodes and the cathode the uncorrected beam energy, could be determined with greater accuracy. However this would most likely only uncover a systematic shift of the absolute resonance energies. Maybe due to the broken extractor a portion of the beam current drains aside the collector, at some point after the trap. As the current is measured at the collector this would go unnoticed. This could be more prominent at higher currents, which would lead to an artificial steepening of the line fitted in Figure 4.5. Still this does not seem plausible as a misaligned beam would result in raising pressures as discussed previously. Another way to dismiss this explanation would be the precise measurement of the current at the cathode. The monitoring output of its PS only provided a fluctuating reading, though the current displayed at the PS itself always was stable and matched the current at the collector within at least 10mA.

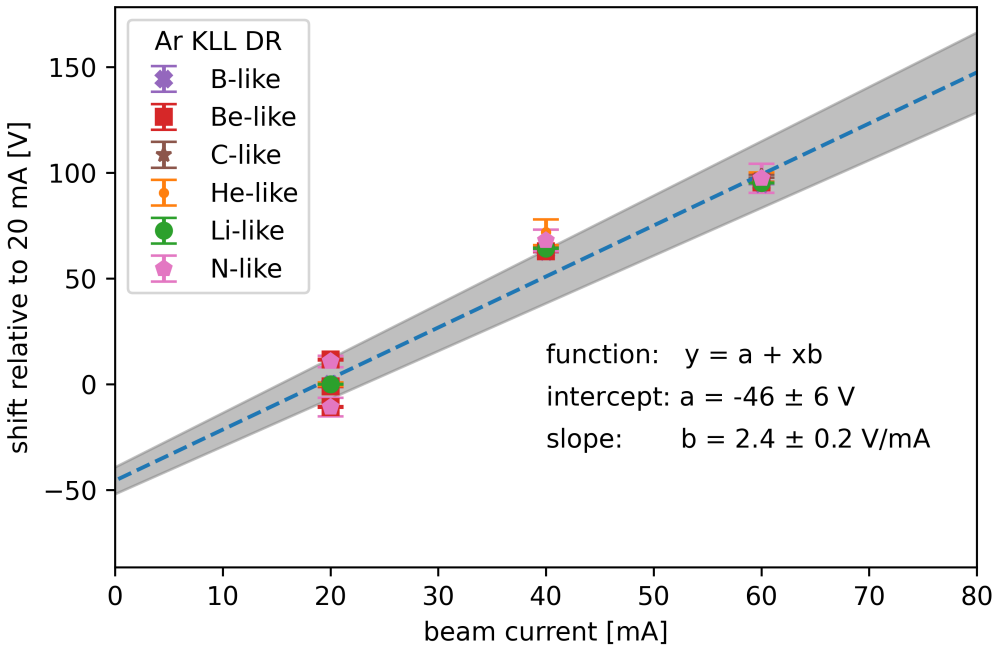

Figure 4.5: The relative offset of the peaks compared to the peaks at 20 mA. The linear fit with given uncertainty by applying the standard errors to the fit.

5 Conclusion and Outlook

5.1 Conclusion

In the scope of this thesis the Hyper-EBIT was successfully recommissioned. The first tests demonstrated currents up to 100mA despite a broken extractor electrode. Everything indicates, that with higher cathode voltages the same cathode could achieve higher currents. With a larger cathode even higher currents would also be possible. Besides the extractor electrode all the independent systems of the Hyper-EBIT, from the magnet over the pressure sensors to the cold head or the cathode heater, proved to be in good working condition.

With the help of a high-purity germanium detector, a set of argon spectra of the KLL dielectric recombination resonance energies could successfully be measured. The distinct peaks originating from different charge states present in the EBIT could be identified. This enabled a characterisation of the change in the effective beam energy due to the electron beams space charge potential V_e. The results of the relative shift between measurements at different beam currents resulted in the following value:

$$\Delta V_e = (2.4 \pm 0.2) \frac{\mathrm{V}}{\mathrm{mA}}.$$

Due to the suddenly occurring defect of the IGLET detector, broader investigation into the shift due to the ions could not be conducted. Going forward, a more exact measurement of the applied voltage to the drift tubes with a precise voltage divider would allow to put limits on certain systematic effects. Also a more sophisticated measurement of the electron beam current should be conducted.

5.2 Outlook

For the future application of the Hyper-EBIT it is of great importance to enable its operation at HV. An already designed HV-platform goes into production within the next few weeks. Then the gun manipulator and all the PS of the gun can be installed on it. The safety of operators and surrounding technical equipment will be assured by the installation of a spacious HV cage around this platform. Furthermore, due to the limited distance to the cold head cryocooler, a gas tank around the collector becomes necessary to improve the breakdown voltage. Once this tank is installed, the extractor electrode can be fixed as well. Inside the trap the ion production can be improved by introducing a new drift tube setup, where no insulating materials are "visible" to the ions. Moreover, the design of the electrode stack will be simplified by removing the octopol electrodes of the central trap [33].

Appendix

Table 5.1: Fitted KLL dielectric recombination energies of argon

(a) 20 mA measurement

Charge state	E_{beam} [eV]	error [eV]
He	2319.27	0.60
Li	2377.00	0.11
Be	2408.62	0.24
Be	2418.46	0.33
Be	2431.07	0.27
B	2467.90	0.07
C	2514.43	0.25
N	2549.32	3.57
N	2570.88	0.73
O	2606.36	13.69

(b) 40 mA measurement

Charge state	E_{beam} [eV]	error [eV]
He	2391.18	6.08
Li	2441.24	0.19
Be	2482.27	0.11
B	2530.58	0.14
C	2579.00	0.70
N	2628.07	4.44

(c) 60 mA measurement

Charge state	E_{beam} [eV]	error [eV]
He	2417.23	2.20
Li	2472.27	0.10
Be	2514.85	0.10
B	2562.72	0.12
C	2612.87	0.75
N	2657.51	6.32

(d) 75 mA measurement

Charge state	E_{beam} [eV]	error [eV]
He	2404.00	3.76
Li	2466.39	0.14
Be	2508.78	0.19
B	2556.46	0.39
C	2609.76	1.46
N	2662.00	7.56

Figure 5.1: KLL DR resonance spectrum of Ar^{16+} to Ar^{10+} ions

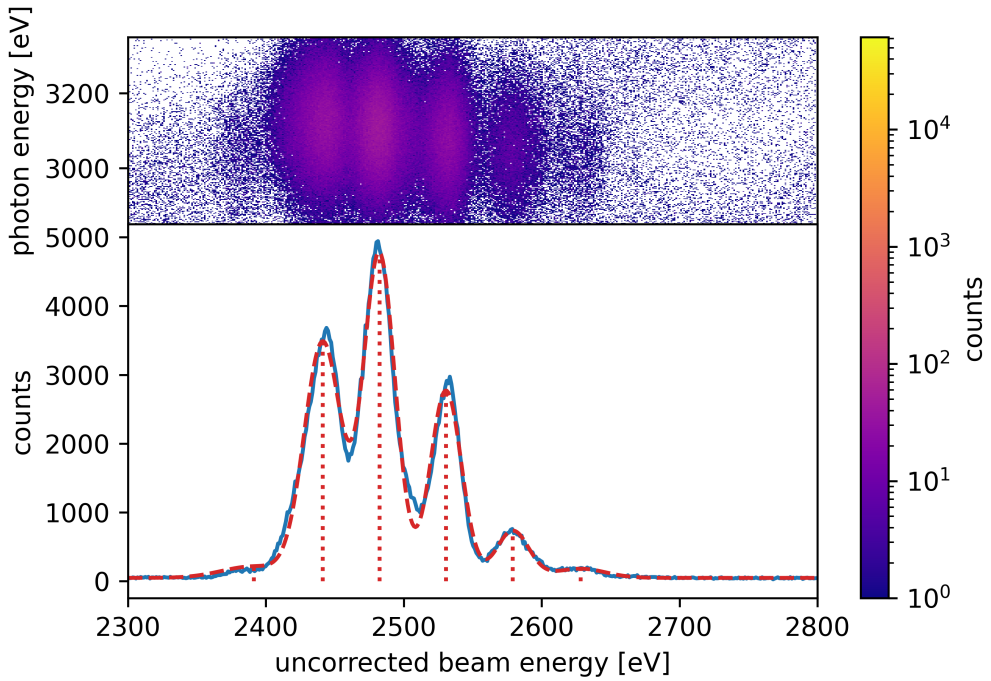

(a) 40 mA measurement

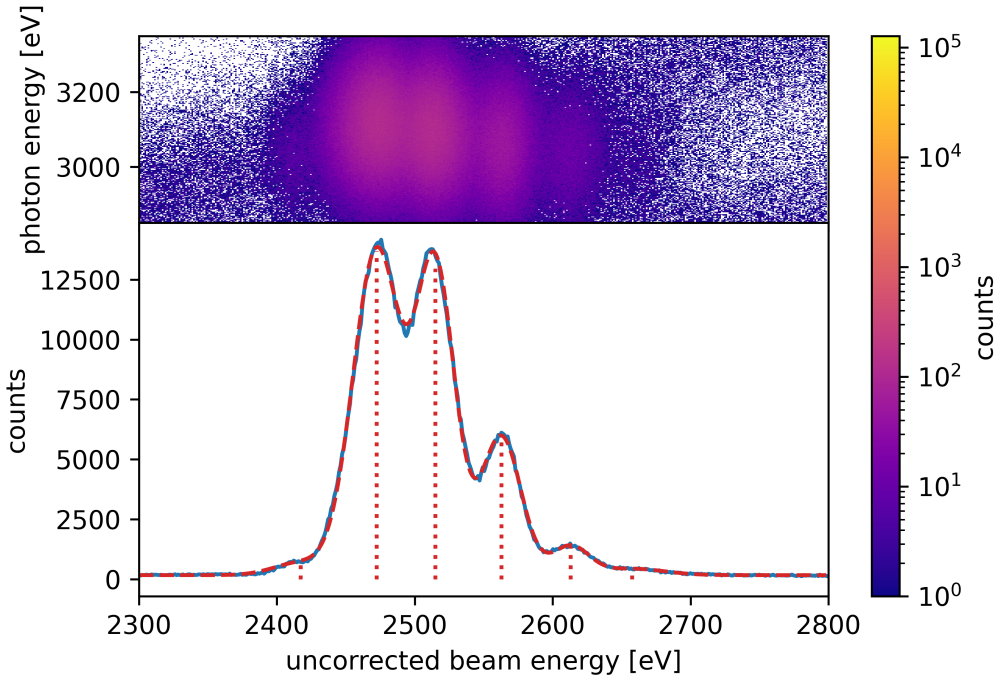

(b) 60 mA measurement

Bibliography

1. *Fundamentals of Plasma Physics* Third Edition (ed Bittencourt, J. A.) (Springer-Verlag New York, Inc., 2004).
2. Beier, T. The gj factor of a bound electron and the hyperfine structure splitting in hydrogenlike ions. *Physics Reports* **339** (2000).
3. Sturm, S. *et al.* The ALPHATRAP experiment. *The European Physical Journal Special Topics* **227** (2019).
4. Rischka, A. *et al.* Mass-difference measurements on heavy nuclides with at an eV/c2 accuracy level with PENTATRAP (2022).
5. Bergström, I. *et al.* SMILETRAP—A Penning trap facility for precision mass measurements using highly charged ions. *Nuclear Instruments and Methods in Physics Research Section A: Accelerators, Spectrometers, Detectors and Associated Equipment* **487** (2002).
6. Levine, M. A., Marrs, R. E., Henderson, J. R., Knapp, D. A. & Schneider, M. B. The Electron Beam Ion Trap: A New Instrument for Atomic Physics Measurements. *Physica Scripta* **T22** (1988).
7. Becker, R. & Kester, O. Electron beam ion source and electron beam ion trap (invited). *Review of Scientific Instruments* (2010).
8. Micke, P. *et al.* The Heidelberg compact electron beam ion traps. *Review of Scientific Instruments* **89** (2018).
9. Marrs, R. E., Elliott, S. R. & Knapp, D. A. Production and Trapping of Hydrogenlike and Bare Uranium Ions in an Electron Beam Ion Trap (1994).
10. López-Urrutia, J. R. C. *et al.* Progress at the Heidelberg EBIT. *Journal of Physics: Conference Series* **2** (2004).
11. Martínez, A. J. G., López-Urrutia, J. R. C., Fischer, D., Orts, R. S. & Ullrich, J. The Heidelberg EBIT: Present Results and Future Perspectives. *Journal of Physics: Conference Series* **72** (2007).
12. Demtröder, W. *Atoms, Molecules and Photons* (Springer Berlin Heidelberg, Berlin, Heidelberg, 2018).
13. Dobrodey, S. *Charge-exchange studies of bare and hydrogen-like low-Z ions in the X-ray and extreme-the X-ray and extreme-ultraviolet ranges inside an electron beam ion trap* PhD Thesis (University of Heidelberg, 2019).
14. Beilmann, C. *et al.* Prominent higher-order contributions to electronic recombination. *Physical review letters* **107** (2011).

15. Beiersdorfer, P. A "brief" history of spectroscopy on EBIT. *Canadian Journal of Physics* **86** (2008).

16. Schweiger, C. *Construction and commissioning of a room-temperature electron beam ion trap and development of a wire probe injection system* Master Thesis (University of Heidelberg, 2017).

17. Brillouin, L. A Theorem of Larmor and Its Importance for Electrons in Magnetic Fields. *Physical Review* **67** (1945).

18. Herrmann, G. Optical Theory of Thermal Velocity Effects in Cylindrical Electron Beams. *Journal of Applied Physics* **29** (1958).

19. Currell, F. & Fussmann, G. Physics of Electron Beam Ion Traps and Sources (2005).

20. Baumann, T. *Spektroskopische Untersuchungen resonanter Rekombinationsprozesse an hochgeladenem Silizium in einer Elektronenstrahl-Ionenfalle* Doktorarbeit (Universität Heidelberg, 2012).

21. *Solid state physics* (eds Hunklinger, S. & Enss, C.) (De Gruyter, Berlin and Boston, 2022).

22. Warnecke, C. *The CANREB Electron Beam Ion Source: Assembly, Characterisation and first Tests* Bachelor Thesis (University of Heidelberg, 2017).

23. Heider, M. B. *Performance and stability tests of bare high purity germanium detectors in liquid argon for the GERDA experiment* PhD thesis (University of Heidelberg, 2009).

24. Cronin, J. *Modern dispenser cathodes* 1981.

25. Pierce, J. R. Rectilinear Electron Flow in Beams. *Journal of Applied Physics* **11** (1940).

26. Mandal, P., Sikler, G. & Mukherjee, M. Simulation study and analysis of a compact einzel lens-deflector for low energy ion beam. *Journal of Instrumentation* **6** (2011).

27. *Quality Assurance Data Sheet: IGLET-X Series* 1999.

28. ORTEC. *Model 672 Spectroscopy Amplifier Operating and Service Manual* 2002.

29. Khan, F., Khandelwal, G. S. & Wilson, J. W. 1s2 1S-1s np 1P TRANSITIONS OF THE HELIUM ISOELECTRONIC SEQUENCE MEMBERS UP TO Z = 30. *The Astrophysical Journal* (1988).

30. Saloman, E. B. Energy Levels and Observed Spectral Lines of Ionized Argon, Ar II through Ar XVIII. *Journal of Physical and Chemical Reference Data* **39** (2010).

31. López-Urrutia, J. C. *Exploration of DR-resonances: D-J03-2.1* 2008.

32. Zou, Y., Crespo López-Urrutia, J. R. & Ullrich, J. Observation of dielectronic recombination through two-electron–one-photon correlative stabilization in an electron-beam ion trap. *Physical Review A* **67** (2003).

33. Blessenohl, M. A. *et al.* An electron beam ion trap and source for re-acceleration of rare-isotope ion beams at TRIUMF. *The Review of scientific instruments* **89** (2018).

Erklärung

Ich versichere, dass ich diese Arbeit selbstständig verfasst und keine anderen als die angegebenen Quellen und Hilfsmittel benutzt habe.

Heidelberg, den September 24, 2022,